POLITECNICO
MILANO 1863

DIPARTIMENTO DI MECCANICA

mecc

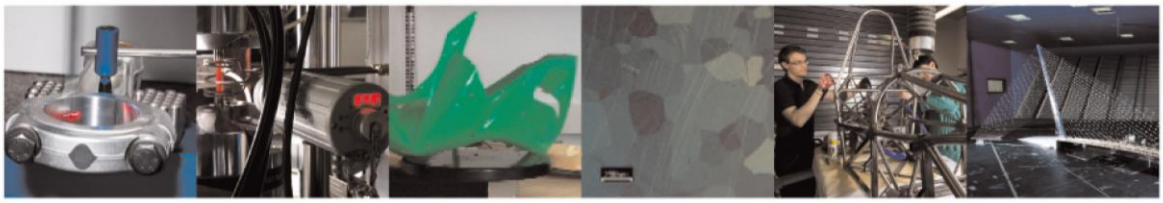

Fast optimisation procedure for the selection of L-PBF parameters based on utility function

Stefania Cacace, Quirico Semeraro

This is an Accepted Manuscript of an article published by Taylor & Francis in Virtual and Physical Prototyping on 16 Nov 2021, available online:
https://doi.org/10.1080/17452759.2021.1998871

This content is provided under CC BY-NC-ND 4.0 license

DIPARTIMENTO DI MECCANICA ■ POLITECNICO DI MILANO
via G. La Masa, 1 ■ 20156 Milano ■ EMAIL (PEC): pecmecc@cert.polimi.it
http://www.mecc.polimi.it
Rev. 0

ARTICLE TEMPLATE

Fast optimization procedure for the selection of L-PBF parameters based on utility function

ARTICLE HISTORY
Compiled October 27, 2021

ABSTRACT
The selection of the process parameters in L-PBF processes is crucial because the mechanical properties of the printed part depend on them. However, the procedure for selecting these parameters can be expensive from an experimental point of view. Therefore, it is necessary to identify simplified models that allow fast and reliable optimization. Furthermore, the choice of parameters cannot be based exclusively on qualitative aspects but must also consider the productivity of the process to obtain a satisfactory compromise. This paper proposes a procedure for selecting parameters based on a semi-analytical thermal model, which, together with a geometric-based defect model allows identifying an optimality region where good solidification and productivity are considered. The optimization is carried using a properly defined utility function. The procedure is validated through the production of AISI 316L specimens using an industrial L-PBF system.

KEYWORDS
Laser Powder Bed Fusion; optimization; process parameters; productivity; analytical models; simulation

1. Introduction

Metal additive manufacturing (AM) technologies are emerging to produce complex parts for aerospace, tools, and biomedical sectors. Among metal additive manufacturing technologies, Laser Powder Bed Fusion (L-PBF) is one of the most promising in terms of customization, part mechanical properties, and design freedom. The interest in the performances of metal AM parts is due to the high-impact applications where these technologies are used, such as maritime (Li et al. 2021), aerospace (Pradeep et al. 2021), and electronics (Mezghani et al. 2021). Further research is needed to improve the final part quality and reliability to allow a wider implementation of L-PBF technologies in these critical sectors. One of the limits of L-PBF is the development of the optimal set of process parameters to obtain a good solidification and therefore high mechanical properties. Studies have shown that the number of process parameters to be selected is large (Spears and Gold 2016; O'Regan et al. 2016); however, the vast literature has shown that only a subset of these parameters is responsible for a good solidification process (Pragana et al. 2020; Kurzynowski et al. 2018; Rao et al. 2016; Dilip et al. 2017). In detail, energy density E_d (J/mm^3) is an established index to predict the density of L-PBF parts (Wang et al. 2016; Prashanth et al. 2017; Karimi et al. 2018; Liu et al. 2020). Energy density is defined as:

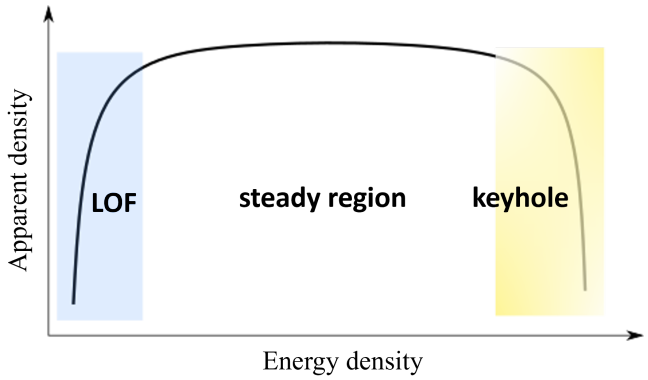

Figure 1. Relationship between energy density and part density

$$E_d = \frac{P}{v \cdot H \cdot L} \tag{1}$$

where P is the laser Power (W), v is the laser speed (m/s), H is the hatch distance (μm) and L is the layer thickness (μm). The relationship between energy density and part density is shown in Figure 1. This trend has been identified for different materials, for example AISI 316L (Lavery et al. 2017), AlSi10Mg (Hyer et al. 2020), Ti6Al4V (Han et al. 2017), and copper (Jadhav et al. 2021). In general, low energy density values result in a lack of fusion porosity, i.e. the energy is insufficient to melt the powder layer properly. Extremely high energy density values produce keyhole porosity induced by the highly irregular molten metal flow (King et al. 2014). Balling is a well-known defect occurring at low energy density when high scan speed and high power are used (Scime and Beuth 2019). Based on the literature review, only a few documents find a clear correlation between the final part of balling at low energy density and defects. According to Li et al. (2012), the effect of balling on the laser track formation is an increased surface roughness of the printed surface; the re-melting of the next layer might remove these irregularities.

The optimization of process parameters also needs to consider other peculiarities of the L-PBF process, such as productivity. L-PBF are almost three times less productive than standard methods (Sun et al. 2016; Gutowski et al. 2017); to speed the process, it is possible to select a proper combination of process parameters (or energy density) which allows maximizing the Build Rate (Tang et al. 2019). The Build Rate, BR (cm^3/h), is defined as in Eq. (2).

$$BR = H \cdot L \cdot v \tag{2}$$

The maximization of the BR refers to a faster laser movement, which corresponds in Figure 1 to move towards low energy density and, eventually, the increased probability of producing parts with a specific type of porosity, i.e. lack of fusion. So, for this reason, this paper focuses on this particular type of porosity that has been widely recognized as one of the leading causes of reduced mechanical properties in L-PBF parts (Snow, Nassar, and Reutzel 2020).

The approaches available for the selection of the optimal parameters can be experi-

mental (Pfaff et al. 2020) or based on computational methods (Bayat, Mohanty, and Hattel 2019), clearly also combined approaches are possible (Letenneur, Kreitcberg, and Brailovski 2019).Analytical thermal models have been widely used among computational methods because of their easy implementation and fast simulation times (Yan et al. 2020). These models describe the thermal field induced by the laser determining the size of the molten pool; the thermal field depends on the process parameters used, power and laser speed.
The melt pool size and geometry data can be used to predict the formation of different types of porosity. According to the defect model proposed by Tang, Pistorius, and Beuth (2017), the lack of fusion porosity is formed when the width (W) of the molten pool is smaller than the distance between consecutive molten tracks (H), or when the molten pool depth (D) is smaller than the layer thickness (L). A graphical representation of this relationship is represented in Figure 2. According to this model, the melt pool is approximated by a dual half-elliptical cross-sectional shape and the condition for lack of fusion formation can be expressed with the following relationship:

$$\left(\frac{H}{W}\right)^2 + \left(\frac{L}{D}\right)^2 \leq 1 \tag{3}$$

Eq. (3) is described graphically a quarter of a circumference with unit radius in the plane (H/W) and (L/D), as shown in Figure 3. All conditions (P,v,H,L) that belong to the colored area in Figure 3 do not result in lack of fusion porosity.

The combination of analytical models for melt pool size prediction and geometrical-based models for predicting porosity can be used to assess the printability of the materials in a pre-defined region of the parameters and eventually define an optimal set of processing conditions considering both solidification and productivity criteria. Other authors proposed procedures for the selection of process parameters for L-PBF processes. Pfaff et al. (2020) provide an experimental approach to identify a large set of parameters, including the scanning strategy and near-surface parameters. The procedure is entirely experimental and requires iterative designs of the experiments. Tang et al. (2019) used his geometric-based model for lack of fusion porosity to identify one optimal set of process parameters with increased productivity. Letenneur, Kreitcberg, and Brailovski (2019) used a combination of melt pool models and experiments to identify processing maps for different materials. Tang et al. (2019) used the defect model proposed in his previous work, predicted the fraction of lack of fusion porosity, and fabricated AlSi10Mg parts with a double build rate compared to the standard condition.
However, all these models do not consider the inevitable variability of L-PBF processes which is one of the main concerns of L-PBF technologies compared to traditional manufacturing processes (Dowling et al. 2020). Therefore, the variability of the melt pool size is the focus of the present work.

Melt pool instabilities and a non-homogeneous powder bed could induce large variability in the melt pool sizes estimated using deterministic thermal models (Chen et al. 2019, 2020, 2021). In addition, the hypotheses on which analytical thermal models are based induce errors in the estimation of the melt pool size (Yan et al. 2020; Devesse, De Baere, and Guillaume 2014). These errors can be accounted for considering the variability when predicting porosity, avoiding thus using more complex models. For this reason, we propose a procedure that considers the variability of melt pool size in the selection of the optimal process parameters for L-PBF. Contrary to the literature, the result of the procedure is a probability of lack of fusion porosity. The selection

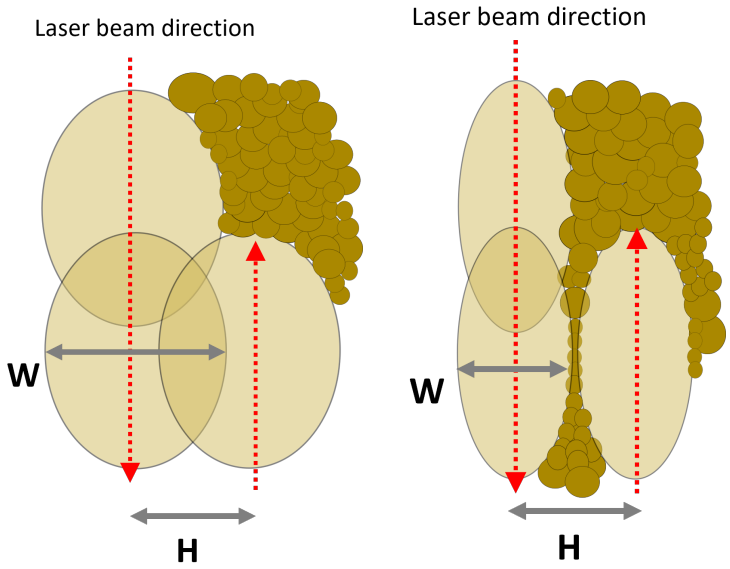

(a) Good solidification. (b) Lack of fusion defect

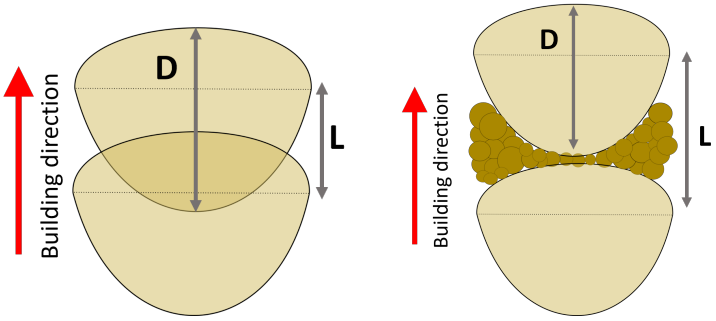

(c) Good solidification. (d) Lack of fusion defect

Figure 2. Representation of the lack of fusion porosity accordint to the model proposed by Tang, Pistorius, and Beuth (2017). (a) and (b) Top view of the effect of hatch distance (H) and melt pool width (W), (c) and (d) lateral view of the effect of layer thickness (L) and melt pool depth (D) on the solidification of the printed parts.

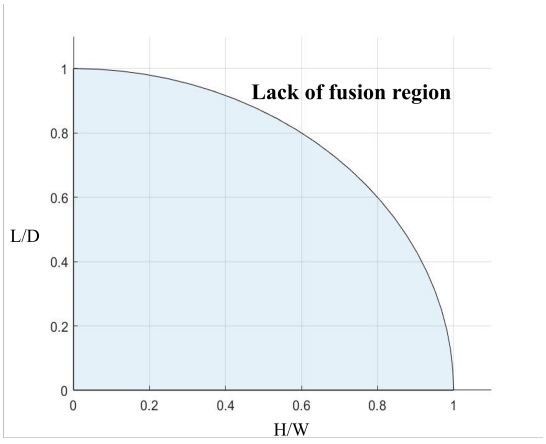

Figure 3. Lack of fusion constraint according to Eq. 3. The colored area indicates the conditions that ensure a good bonding between scan tracks.

of the optimal set of the parameters is based on a utility function, which combines the minimization of the lack of fusion probability and maximization of productivity. The resulting set of parameters ensures that high-dense parts are produced, avoiding the lack of fusion porosity. The methodology was conceived considering that optimal process parameters are not known before printing and that a costly experimental campaign covering an extensive variation of parameters is not feasible from an industrial point of view. The information required for the methodology presented here is the material physical properties and an estimate of the variability of the melt pool. The output of the proposed procedure is a utility function that, when maximized, provides information on the optimal set of process parameters. An experimental campaign using AISI 316L printed samples was carried out to validate the ability of the procedure to identify the lack of fusion region and the optimal set of process parameters.
The paper is organized as follows: in Section 2 the thermal model and the defect model are described; following in Section 3 the overall workflow is detailed described; in Section 4 the experimental campaign for the procedure validation is reported. The results of the procedure and the validation samples results are reported in Section 5.

2. Methodologies

2.1. *Melt pool model*

The melt pool model used for the calculations of the melt pool dimensions is derived from King et al. (2014) and Rubenchik, King, and Wu (2018) and it is based on the Rosenthal equation. This model was successfully used to predict the melt pool size for different materials such as AISI 316L, Ti6Al4V and AlSi10Mg (King et al. 2014; Tang et al. 2019; Promoppatum and Yao 2019).

$$T = \frac{AP}{\pi k}\sqrt{\frac{D}{\pi}}\int_0^\infty \frac{exp\left[-\frac{z}{4Ds} - \frac{y+(x-s)^2}{(4Ds+a^2)}\right]}{(4Ds+a^2)\sqrt{t}}\,ds \tag{4}$$

The quantities in Eq. (4) are defined as follows: a (m) is the laser radius and α (m^2/s) is the thermal diffusivity of the material (m^2/s), A is the laser absorptivity, c_p is the heat capacity (J/Kg/K), ρ is the density of the material (kg/m^3). The analytical solution was improved by the normalization of parameters introduced by Rubenchik, King, and Wu (2018), leading to Eq.(5).

$$g = \int_0^\infty \frac{exp\left[-\frac{z'}{4t} - \frac{y'+(x'-t)^2}{(4pt+1)}\right]}{(4pt+1)\sqrt{t}}\,dt \tag{5}$$

$$p = \frac{\alpha}{v\sigma} \qquad x' = \frac{x}{\sigma} \qquad y' = \frac{y}{\sigma} \qquad z' = \frac{z}{\sqrt{\frac{\alpha\sigma}{v}}} \qquad T_s = \frac{AP}{\pi\rho c_p\sqrt{\alpha v a^3}}$$

Function g is defined as the ratio between the estimated temperature and the temperature at the center of the moving spot, $g = T/T_s$ in function of spatial coordinates (x, y, z). The melt pool dimensions are obtained when the thermal field

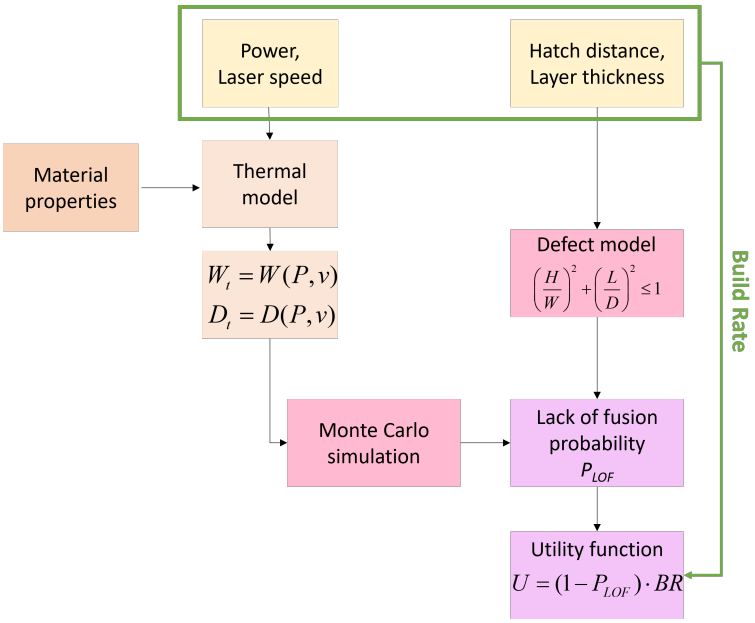

Figure 4. Procedure workflow for the selection of the optimal processing parameters

is equal to the melting temperature, i.e. $T = T_m$ in the numerator of function g.

2.2. *Defect model for lack of fusion*

The model proposed by Tang, Pistorius, and Beuth (2017) states that the condition for avoiding the lack of fusion porosity is that the melt pool width is larger than the hatch space, see Figure 2 (a) and (b); and that the melt pool depth is larger than the layer thickness, as shown in Figure 2 (c) and (d). Thus, if the combination of the process parameters (H, L) and the melt pool dimension (W, D) does not meet the condition in Eq (3), lack of fusion porosity is formed in the final part, which eventually indicates that the Energy density is not high enough to allow a complete solidification.

3. Procedure workflow

The proposed procedure workflow is presented in Figure 4. In this section, for each step a detailed description of the procedure is carried out.

3.1. *Determination of the range of parameters to be investigated*

The procedure starts with defining a range of possible power values, laser speed, and hatch distance. Layer thickness L is considered constant because it is usually predefined by the machine manufacturer based on the material used. In any case, the procedure is easily generalized also in case the layer thickness is varied. This range can be derived from previous literature or is defined based on the minimum, and maximum values set based on the industrial L-PBF system considered. In the case of

the present work, the investigated range of parameters is reported in Table 1. This range was based on the suggested parameters of the machine manufacturer for AISI 316L and on the range allowed by the L-PBF system used.

Table 1. Range of the process parameters considered in this study.

Parameter	Value
Power	150 - 200 W
Hatch distance	75 - 130 μm
Speed	0.1 - 1.5 m/s
Layer thickness	50 μm
Pre-heating	none

3.2. *Melt pool size estimation using simulated experiments*

A simulation campaign based on a design of the experiment approach is used to derive melt pool depth (D) and width (W) in the investigated region of the parameters using the thermal model described in Section 2.1. Melt pool size depends only on power and scan speed; an experimental design was designed by diving the ranges of power and speed in equispaced intervals (10 W for Power, 0.2 m/s for speed). The levels used for the simulation campaign are reported in Table 2.

The output of this simulation campaign is a set of melt pool depth D and width W for each combination of power and laser speed considered. The simulated data are then used to build two regression models predicting melt pool depth and width in the region of parameters of interest, such as the ones in Eq. (6).

$$\begin{aligned} D_t &= D(P, u) \\ W_t &= W(P, u) \end{aligned} \tag{6}$$

The material used to validate the procedure is AISI 316L and the physical properties needed to evaluate the melt pool size are reported in Table 3.

3.3. *Monte Carlo simulation*

A Monte Carlo approach was used to incorporate the variability in the procedure. The procedure assumes that for each combination (P,v) the melt pool depth and width variability is described by a multivariate gaussian distribution with mean $\boldsymbol{\mu} = [D_t, W_t]$ and variance-covariance matrix $\boldsymbol{\Sigma_{DW}}$.

$$(W_i, D_i) \sim MN(\boldsymbol{\mu}, \boldsymbol{\Sigma_{DW}}) \tag{7}$$

Table 2. Factorial simulated experiment for melt pool size estimation.

Parameter	Value
Power	150, 160, 170, 180, 190, 200 W
Speed	0.1, 0.3, 0.5, 0.7, 0.9, 1.1, 1.3, 1.5 m/s

Table 3. Room temperature AISI 316L physical properties (King et al. 2014).

Property	Value	MU
Heat Capacity	460	J/kg/K
Density	7980	kg/m^3
Melting temperature	1673	K
Absorption	0.35	-
Thermal diffusivity	5.38 e-06	m^2/s

The mean vector $\boldsymbol{\mu}$ is the results of the set of Eq. (6) for a specific combination of (P,v); the variance-covariance matrix $\mathbf{\Sigma_{DW}}$ was estimated based on a preliminary experimental campaign.

$$\mathbf{\Sigma_{WD}} = \begin{bmatrix} 3.3887 & 0 \\ 0 & 6.6100 \end{bmatrix}$$

The covariance between melt pool depth and width, σ_{WD} (i.e., the non-diagonal elements in $\mathbf{\Sigma_{DW}}$) is the most challenging quantity to estimate, for this reason, a sensitivity analysis is carried out to investigate how the covariance influences the procedure and, therefore, the selection of the optimal set of parameters. For the sensitivity analysis, two covariance values are selected: one positive (+4.3) and one negative (-4.3).

The number of simulated melt pools is 50000 for each combination of input parameters.

3.4. *Lack of fusion probability*

The defect model by Tang, Pistorius, and Beuth (2017) allows to predict the formation of lack of fusion porosity based on four parameters: hatch distance, melt pool width, layer thickness, melt pool depth. In its original definition, each combination (H,W,L,D) defines a point in the space defined by (H/W) and (L/D) as shown in Figure 3. If the point satisfies the constraint in Eq. (3), a proper solidification is expected.

When considering the variability due to Monte Carlo simulation, the defect model constraint is to be modified. Several melt pool sizes (W,D) are generated for each set of input parameters according to the multi-variate normal distribution model defined in Eq.7. The random generation of melt pool width and depth values results in a set of points in the space (H/W) and (L/D); these sets of points are represented as black dots in Figure 5 (a). It is not possible to determine if the specific input condition results in a lack of fusion porosity, but a probability of lack of fusion is derived.

When all the generated data belong to the feasible region (black dots in Figure 5 (a)), P_{LOF} is equal to 0. In some conditions, the generated data are on the constraint defined by Eq. 3 (grey dots in Figure 5 (a)). In this case, P_{LOF} is given by the number of generated data outside the constraint (red dots in Figure 5 (b)) divided by the total number of generated data. The shape of the generated data (black and grey dots) illustrated in Figure 5 depend on the hypothesized model, in this case the multivariate normal distribution. In detail, the the ellipse center is the mean of the generated data $\boldsymbol{\mu}$, which is the results of the set of Eq. (6). The length of the ellipse axis depends on the variances of the melt pool depth and width, which are the

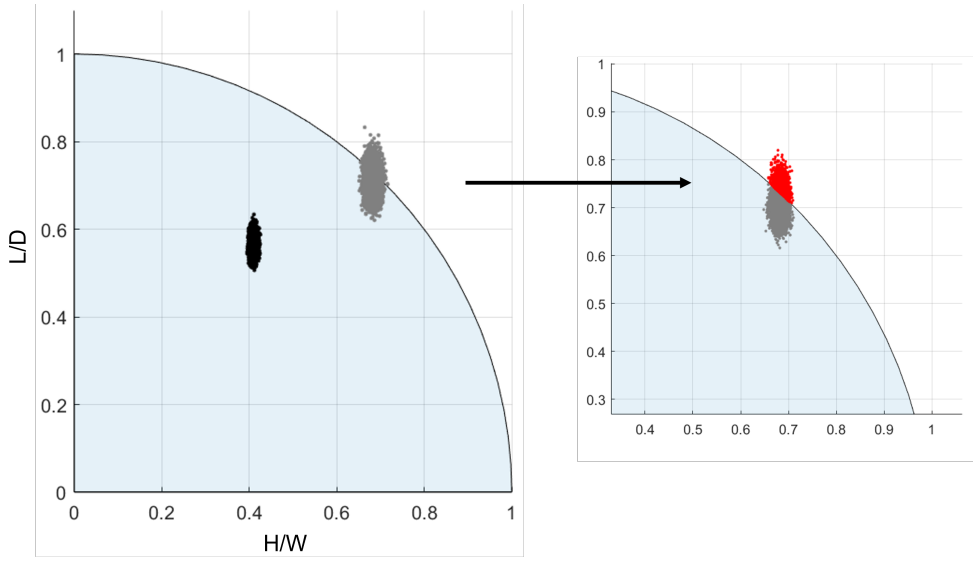

Figure 5. Results of the Monte Carlo generation of melt pool according to model in Eq.7. When the generated data belong entirely in the acceptange region, P_{LOF} is zero (black dots). When the generated data are on the constraint (gray dots), P_{LOF} is evaluated as the number of conditions that do not satisfy the constraint (red dots) over the total number of simulated data (magnified image on the right).

diagonal elements of the matrix $\mathbf{\Sigma_{DW}}$. Finally, the orientation of the ellipse depends on the sign and value of the covariances, i.e., the non-diagonal elements of the matrix.

3.5. *Utility functions*

The objective of the selection of process parameters (P,v,H,L) is based on the maximization of the Build Rate subject to the minimization of the lack of fusion probability:

$$\begin{aligned} \max_{v,H} \quad & BR(v,H,L) \\ \text{s.t.} \quad & P_{LOF}(P,v,H,L) \leq P_{LOF,0} \end{aligned} \tag{8}$$

where $P_{LOF,0}$ defines the maximum probability we would like to accept for lack of fusion formation. The experimenter selects this value depending on the performances required in the final part; obviously, choosing a higher probability of lack of fusion would lead to a higher build rate. This approach has two main drawbacks. The first one is that selecting the value of $P_{LOF,0}$ is tricky and not straightforward. The second is that the output of such a problem, as defined in Eq. 8, provides one combination of parameters, and it does not show how the solution changes depending on the factors involved.
So, instead of solving a constrained problem, utility functions can be used (Walsh et al. 2004; Mosa and Paton 2016). The utility function considered in this work is the following:

$$u(P,v,H,L) = [1 - P_{LOF}(P,v,H,L)] \cdot BR(v,H,L) \tag{9}$$

Similarly, the optimization problem in Eq. (8) can be re-written using the utility

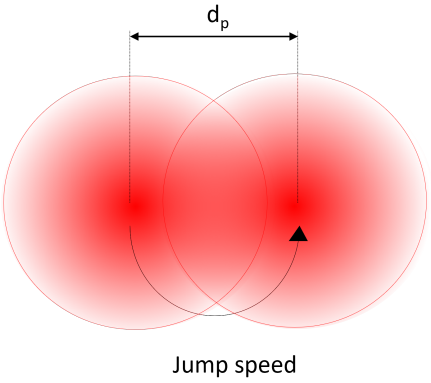

Figure 6. Definition of jump speed to convert point distance and exposure time to laser speed

function and solving the easier optimization problem defined in Eq. (10).

$$\max_{P,v,H,L} \quad u(P, v, H, L) \tag{10}$$

4. Validation samples

Validation samples were built using Renishaw AM250 industrial L-PBF system and AISI 316L steel powder. The machine is equipped with a laser working in pulsed mode and the laser spot is approximately 70 μm. In pulsed lasers, the laser speed is a function of two other parameters: point distance d_p and exposure time t. The following relationship was used to convert point distance and exposure time into laser speed:

$$v = \frac{d_p}{\frac{dp}{JS} + t} \tag{11}$$

Jump speed (JS) is the speed at which the laser moves from one spot to the other along the same scan line (as shown in Figure 6); the JS was set at 8000 mm/s. The process parameters varied in the experimental campaign were power, exposure time, hatch distance, and point distance. An extensive range of process parameters was selected, and three different energy density levels were considered in this study (34, 59 and 103 J/mm^3). The interval of process parameters and the resulting levels of energy density tested is shown in Table 4. The process parameters were selected according to the procedure proposed by Cacace and Semeraro (2018), which allows obtaining different combinations of process parameters resulting in the same level of energy density. The density of the samples was measured using Archimedes' principle.

A total number of 18 different combinations of process parameters were selected. For each combination, two samples were produced. Additionally, four samples using the machine manufacturer suggested conditions for AISI 316L were added to the build (P=200W, d_p=60 μm, d_h=110 μm and t = 80 μs). The density of each sample was measured using the Archimedes method; each measurement was repeated three times and the average density was recorded.

Despite working with a pulsed laser for the printing of the validation samples, small differences are expected. Studies showed that pulsed laser has a slightly smaller melt

Table 4. Process parameters range of the validation samples.

Parameter	Value
Power P	150 W, 200 W
Point distance d_p	34 - 85 μm
Exposure time t	33 - 277 μs
Hatch distance d_h	75 - 124 μm
Speed[a] v	0.15 - 1.1 m/s
Layer thickness L	50 μm (fixed)
Energy density E_d	34, 59, 103 J/mm^3

[a] Derived from Eq.(11) .

pool size (at the same energy density) than continuous. However, the difference becomes significant only when complex geometries are considered (Demir et al. 2019).

5. Results and discussion

5.1. *Melt pool size simulation*

Melt pool width and depth resulting from the simulated factorial experiment described in Section 3.2 are shown in Figure 7. Melt pool width and depth both increase at low speed and high power, that is when the energy deposition increases.

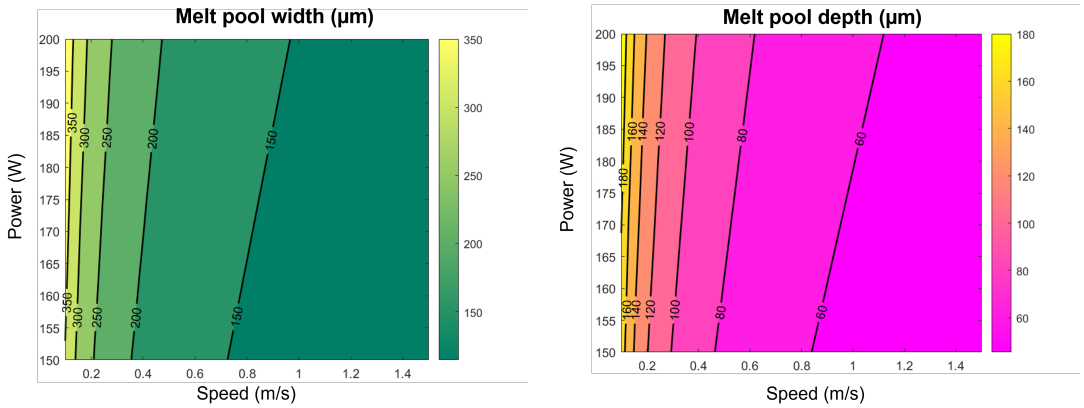

(a) Melt pool width from analytical prediction.

(b) Melt pool depth from analytical prediction.

Figure 7. Melt pool widths and depths obtained from the analytical solutions in Eq.5.

The values obtained from the simulation runs were then used to estimate relationships between melt pool size and process parameters (P,v). The equations are the following:

$$\begin{aligned} D_t &= 2.110 + 4.331\sqrt{(P/v)} \\ W_t &= 33.62 + 8.089\sqrt{(P/v)} \end{aligned} \tag{12}$$

These equations showed a high quality fit (adj-R^2 larger than 99% in both cases).

These equations are valid only in the range of parameters considered for the simulated experiment. The coefficients combine the effects of the physical properties of the material, so depending on the values used in the simulations they change. However, the proportionality between melt pool size and $\sqrt{(P/v)}$ is a direct result of Eq. (3).

5.2. *Lack of fusion probability and validation results*

Based on the ranges of the parameters defined in Table 1, for each combination of (P,v,H), melt pool widths and depths are generated according to the model defined Eq.(12). The results are reported in the Appendix. For a specific set of power and speed, the melt pool depth and width were calculated based on the analytical model in Eq. 4. Then, the variability of the melt pool was added using the multivariate normal distribution model according to Eq.7. The probability of lack of fusion is then evaluated for each speed and hatch distance. The derivation of the surface in Figures 8 is derived only based on the thermal properties of the material and the Monte Carlo simulation results. Figures 8 (a) and (b) show the surfaces representing the lack of fusion probability at two power levels. As expected, at low speed and low hatch distance, the lack of fusion probability is zero, which is coherent with Figure 1: at high energy density, the melt pools overlap. At high energy density, other flaws are present, but they are not considered in the procedure as they are produced at extremely low productivity rates.Keyhole porosity arises at large power values combined with low scan speeds, resulting in low build rates. Such a combination of parameters is not obtained using the proposed optimization framework. As shown by Scime and Beuth (2019), the parameters combinations that lead to keyhole are different from those that result in a lack of fusion formation in terms of build rates and combination of power and speed.

The simulation results are that the lack of fusion probability increases sharply as the energy density is reduced.However, in a small range of speed and hatch distances, the probability goes from 0 to 1.The selection of the optimal condition should be carefully optimized because a slight variation in the process parameters significantly affects the mechanical properties.
It also appears that it is possible to use higher values of hatch distance and scan speed (i.e. high build rates) when high power is used.

The density results of the L-PBF samples are used to validate the procedure by verifying that the thermal model combined with the Monte Carlo simulation is able to predict the lack of fusion region. The density results of the validation samples are reported in Table 5; for each of the 18 combinations of the parameters, two samples were printed; while the reference condition was replicated four times.The density results for all samples are reported as % of the reference value for AISi 316L, 7.98 g/cm^3. At E_d= 33 J/mm^3 (lowest level of energy and highest BR) the apparent density values are lower than 94%, indicating the presence of lack of fusion porosity. On the contrary, the reference condition (E_d= 48 J/mm^3) and the other two levels of energy density (59 and 102 J/mm^3) show all high values of density, indicating that they belong to the steady region in Figure 1.
The density results of the printed samples are compared to the predicted region of lack of fusion probability. Figure 8 (c) and (d) show the contour lines of the lack of fusion probability surfaces. The contour lines show the 10, 90, and 100 % probability of lack of fusion formation.

Table 5. Density of AISI 316L validation samples

P (W)	v (m/s)	H (μm)	E_d (J/mm^3)	Density (%)
200	1.16	87	33	93.7%; 93.4%
200	1.29	76		92.3%; 93.2%
200	0.84	124		93.5%; 93.5%
200	0.52	121	59	99.3%;99.4%
200	0.63	99		99.3%; 99.4%
200	0.61	103		99.5%; 99.5%
200	0.48	76	102	99.5%; 99.4%
200	0.31	121		98.9%; 98.7%
200	0.36	103		99.3%; 99.5%
150	0.91	85	33	93.0%; 88.8%
150	0.67	121		93.6%; 93.7%
150	0.79	99		92.3%; 91.7%
150	0.46	102	59	98.9%; 98.9%
150	0.40	121		99.1%; 99.3%
150	0.48	99		99.0%; 99.2%
150	0.34	83	102	98.7%; 99.3%
150	0.25	116		98.1%; 99.2%
150	0.29	96		99.3%; 99.2%
200[a]	0.68	110	48	98.6%; 99.4%; 99.2%; 99.2%

[a] Reference condition.

For each power level, the results of the density samples are reported as dots in correspondence of the specific values of hatch distance and speed indicated in Table 5. Green dots represent samples with an apparent density higher than 98.5%, while red squares represent data with lower densities. The results show that at both levels of power, the procedure predicts the lack of fusion region as all the samples with low density belong to a region where the lack of fusion probability is close to 1.

Since the model has been validated, the utility function can effectively identify the optimal set of process parameters. The function is derived by multiplying the complement of the probability of lack of fusion formation (1-P_{LOF}) (i.e. the probability of good solidification) with the Build Rate, for each speed and hatch distance combination. The utility functions at P=150 W and P=200W are shown in Figure 9 a) and b), respectively. The utility contour lines in Figure 9 c) and d) are derived from the surface defined in Eq. (9) can be used to identify an optimal region of the parameters. First of all, the utility function is maximized at the highest level of power as expected from the definition of BR in Eq. (2), as BR can be rewritten as $BR = P/E_d$. Generally, to maximize productivity, one must choose a high level of power. In other terms, selecting a high power level allows the process to increase by choosing a larger hatch space and a faster speed as the melt pool dimensions also increase with power (see Figure 7). The utility function is reduced when despite the high BR, the formation of porosity is likely, diminishing the "utility" of using those combinations of parameters. By focusing on the highest level of power, the simulation results suggest that the reference condition (indicated in Figure 9 (b)) belongs to the optimal region where the utility is maximized.

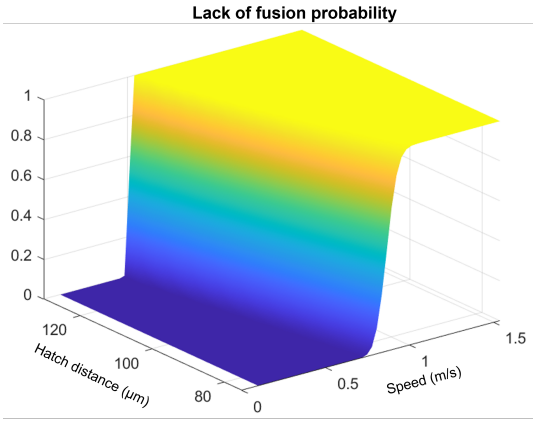

(a) Lack of fusion probability at P = 150 W.

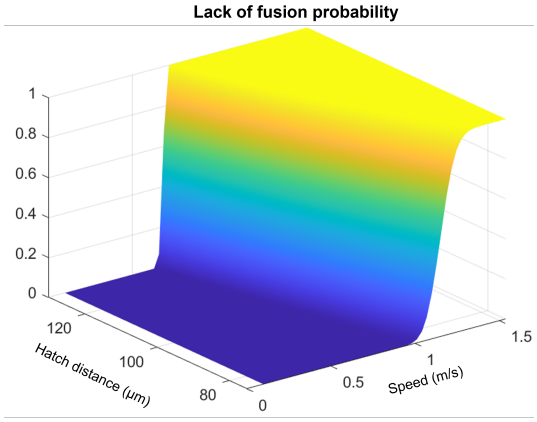

(b) Lack of fusion porosity at P = 200 W.

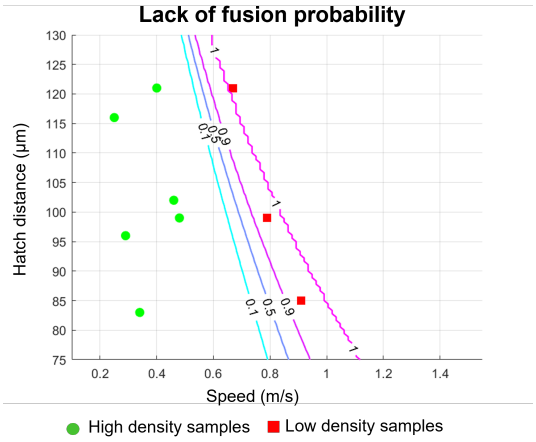

(c) Results of the validation samples at P = 150 W.

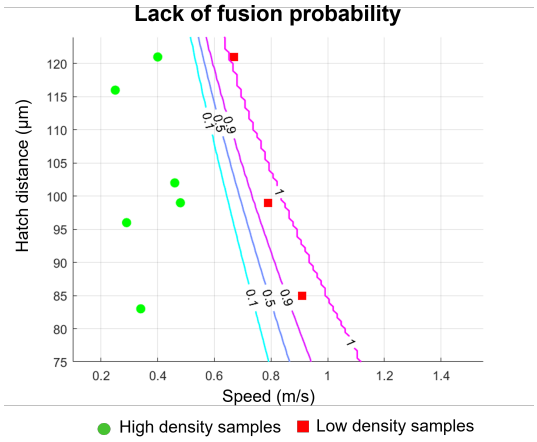

(d) Results of the validation samples at P = 200 W.

Figure 8. (a) and (b) Lack of fusion probability evaluated as function of hatch distance and speed; (c) and (d) Results of the validation samples

Based on the utility function results, all the combinations of speed and hatch distance which result in a utility equal to 4000 (when P is set at 200 W) belong to the optimal set of process parameters. Specifically, the combination of speed and hatch distance with the highest level of utility (equal to 4108) is d_h=114 μm and v=0.72 m/s. Also, the reference condition shows a slightly lower utility value, 3187. The BR of the condition with the highest utility is equal to 14.7 cm^3/h, while the productivity of the reference condition is 13.5 cm^3/h; that means that the new condition allows a 10% increase in productivity without affecting the probability of defect formation.
In conclusion, the utility map was successfully used to determine a new set of process parameters with increased productivity. The utility function (Eq.9) is derived independently from experimental results, and it depends only on the material properties and the variance-covariance matrix. The experimental data provide information on the goodness of the two models used (thermal and defect) because the samples that resulted in a lack of fusion porosity do belong to the predicted region by Tang, Pistorius, and Beuth (2017). Additionally, the reference condition provided by the machine manufacturer is close to the optimal set of parameters identified by the utility map, indicating that the utility map is a valuable tool for fast process optimization.

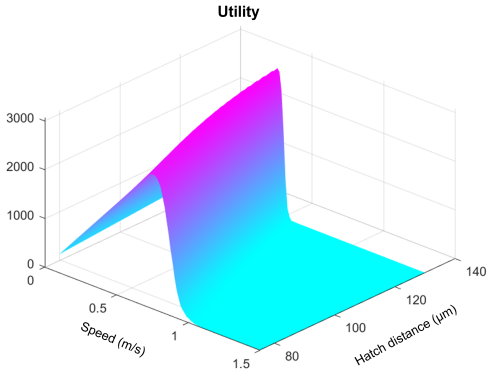

(a) Utility function P = 150 W.

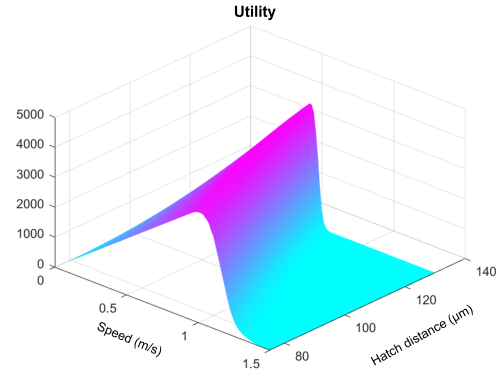

(b) Utility function at P= 200 W.

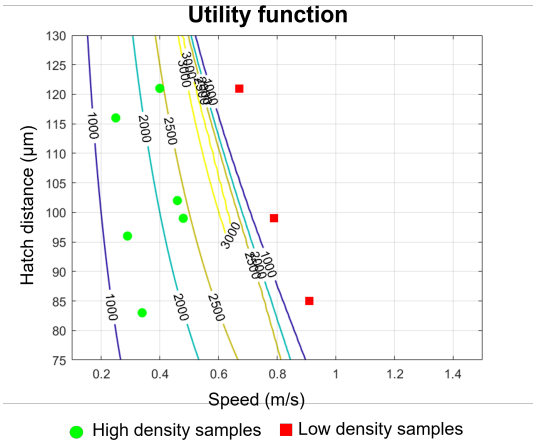

(c) Utility contour plot and result of the validation samples at P=150 W.

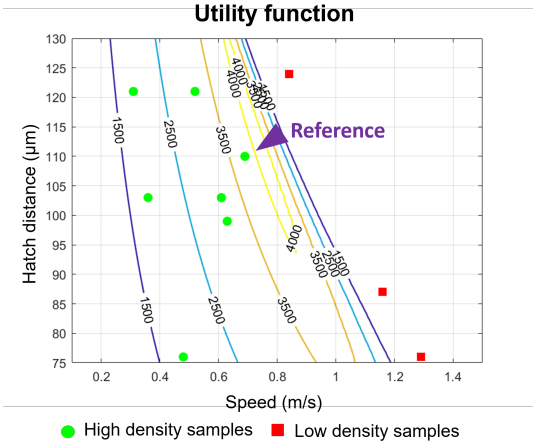

(d) Utility contour plot and result of the validation samples at P=200W.

Figure 9. Utility function and results of the validation samples.

6. Sensitivity analysis

One of the required inputs of the proposed procedure is the selection of the covariance between melt pool depth and width, σ_{WD}. This quantity is difficult to be estimated, and therefore a sensitivity analysis is carried out to investigate the effect of its value on the utility function, and therefore on the optimal processing conditions. Covariance rules the orientation of the generated melt pool in the Monte Carlo simulation; positive covariance indicates a positive correlation between melt pool depth and width; a negative covariance indicates that when melt pool depth increases, the melt pool width decreases, and vice versa.
A representation of the effect of the covariance value on the generation of melt pool depth and width, and therefore on the definition of the lack of fusion probability P_{LOF} is shown in Figure 10.

The procedure for identifying the optimal set of parameters consisted of deriving the utility function using the two values of covariance σ_{WD}=-4.1 and σ_{WD}=+4.1, and comparing them with the case when covariance is equal to 0.

The results of the sensitivity analysis are reported in Table 6. The data show that the covariance has a limited effect on identifying the optimal processing parameters

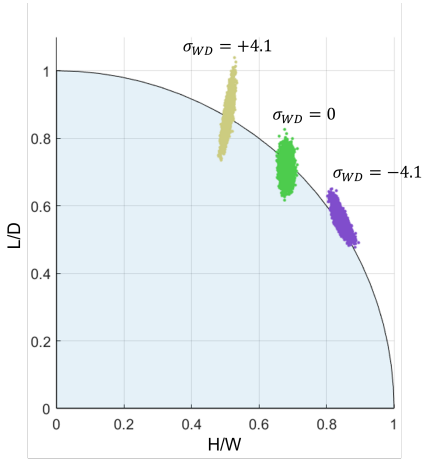

Figure 10. Effect of the covariance value on the generated melt pool values in the Monte Carlo simulation for the determination of the lack of fusion probability P_{LOF}

Table 6. Optimal process parameters and utility results at different σ_{WD} values.

			Optimal process parameters	
	Power (W)	Utility	v (m/s)	d_h (μm)
σ_{WD}=0	200	4108	0.72	114
	150	3077	0.54	115
σ_{WD}=+4.1	200	4012	0.74	112
	150	3011	0.57	109
σ_{WD}=-4.1	200	4166	0.72	117
	150	3123	0.55	114

using the proposed procedure. Given the same power, the utility values are all similar (the differences are in the range of 4%).The maximum difference in the optimal laser scan speed and hatch distance values is 0.03 m/s and 6 μm, respectively .

7. Conclusions

In this work, a fast procedure for selecting of the optimal region of process parameters is proposed. The objective is to find a trade-off between quality (avoid the formation of lack of fusion porosity) and productivity (maximization of the build rate); the multi-objective optimization is solved through a utility function. The procedure exploits semi-analytical thermal models that allow a fast simulation time and good prediction properties. For this reason, the procedure does not require an experimental campaign for tuning the parameters, and the only requested input parameters are the material's physical properties and an estimate of the variance-covariance matrix. The lack of fusion probability is estimated using a geometric-based model proposed in the literature. The natural variability of the melt pool is considered for the first time in this work. A Monte Carlo approach is used to simulate variable melt pool depths and widths to account also for irregularities during the solidification of the melt pool.
Printed samples built at different processing conditions were used to validate the procedure.The model correctly estimated the lack of fusion porosity, and the utility function was used to determine a feasibility region where productivity is maximized,

and the lack of fusion probability is minimized. A new optimal condition is identified that allows a 10% increase in productivity without affecting the probability of defect formation.

Acknowledgement(s)

The Italian Ministry of Education, University and Research is acknowledged for the support provided through the Project "Department of Excellence LIS4.0 - Lightweight and Smart Structures for Industry 4.0".

Disclosure statement

No potential conflic of interest was reported by the authors.

Appendix

Table 7. Melt pool depth and width for the validation samples based on 12

P (W)	v (m/s)	H (μm)	D (μm)	W (μm)
200	1.16	87	59	140
200	1.29	76	56	134
200	0.84	124	69	158
200	0.52	121	87	192
200	0.63	99	79	178
200	0.61	103	81	181
200	0.48	76	90	198
200	0.31	121	112	239
200	0.36	103	104	224
200	0.23	95	131	273
200	0.23	93	129	271
200	0.29	75	117	247
150	0.91	85	58	137
150	0.67	121	67	155
150	0.79	99	62	145
150	0.46	102	80	179
150	0.40	121	86	190
150	0.48	99	79	177
150	0.34	83	94	205
150	0.25	116	109	234
150	0.29	96	101	218
150	0.21	76	117	249
150	0.18	91	128	268
150	0.16	106	137	285
200	0.69	110	76	172

Table 8. List of symbols.

Symbol	Definition	Unit of measurement
P	Power	W
v	Speed	m/s
L	Layer thickness	μm
H	Hatch distance	μm
d_p	Point distance	μm
t	Exposure time	μs
JS	Jump speed	m/s
A	Absoptivity	-
α	Thermal diffusivity	m^2/s
a	Laser radius	μm
c_p	Heat capacity	J/Kg/K
ρ	Density	g/cm^3
T_m	Melting temperature	K
W	Melt pool width	μm
D	Melt pool depth	μm

Nomenclature/Notation

References

Bayat, Mohamad, Sankhya Mohanty, and Jesper Henri Hattel. 2019. "A systematic investigation of the effects of process parameters on heat and fluid flow and metallurgical conditions during laser-based powder bed fusion of Ti6Al4V alloy." *International Journal of Heat and Mass Transfer* 139: 213–230.

Cacace, Stefania, and Quirico Semeraro. 2018. "About fluence and process parameters on maraging steel processed by selective laser melting: Do they convey the same information?" *International Journal of Precision Engineering and Manufacturing* 19 (12): 1873–1884.

Chen, Hui, Yuxiang Chen, Ying Liu, Qingsong Wei, Yusheng Shi, and Wentao Yan. 2020. "Packing quality of powder layer during counter-rolling-type powder spreading process in additive manufacturing." *International Journal of Machine Tools and Manufacture* 153: 103553.

Chen, Hui, Tan Cheng, Qingsong Wei, and Wentao Yan. 2021. "Dynamics of short fiber/polymer composite particles in paving process of additive manufacturing." *Additive Manufacturing* 47: 102246.

Chen, Hui, Qingsong Wei, Yingjie Zhang, Fan Chen, Yusheng Shi, and Wentao Yan. 2019. "Powder-spreading mechanisms in powder-bed-based additive manufacturing: Experiments and computational modeling." *Acta Materialia* 179: 158–171.

Demir, Ali Gökhan, Luca Mazzoleni, Leonardo Caprio, Matteo Pacher, and Barbara Previtali. 2019. "Complementary use of pulsed and continuous wave emission modes to stabilize melt pool geometry in laser powder bed fusion." *Optics & Laser Technology* 113: 15–26.

Devesse, Wim, Dieter De Baere, and Patrick Guillaume. 2014. "The isotherm migration method in spherical coordinates with a moving heat source." *International Journal of Heat and Mass Transfer* 75: 726–735.

Dilip, JJS, Shanshan Zhang, Chong Teng, Kai Zeng, Chris Robinson, Deepankar Pal, and Brent Stucker. 2017. "Influence of processing parameters on the evolution of melt pool, porosity, and microstructures in Ti-6Al-4V alloy parts fabricated by selective laser melting." *Progress in Additive Manufacturing* 2 (3): 157–167.

Dowling, L, J Kennedy, S O'Shaughnessy, and D Trimble. 2020. "A review of critical repeatability and reproducibility issues in powder bed fusion." *Materials & Design* 186: 108346.

Gutowski, Timothy, Sheng Jiang, Daniel Cooper, Gero Corman, Michael Hausmann, Jan-Anders Manson, Timo Schudeleit, et al. 2017. "Note on the rate and energy efficiency limits for additive manufacturing." *Journal of Industrial Ecology* 21 (S1): S69–S79.

Han, Jie, Jingjing Yang, Hanchen Yu, Jie Yin, Ming Gao, Zemin Wang, and Xiaoyan Zeng. 2017. "Microstructure and mechanical property of selective laser melted Ti6Al4V depen-

dence on laser energy density." *Rapid Prototyping Journal* .

Hyer, Holden, Le Zhou, Sharon Park, Guilherme Gottsfritz, George Benson, Bjorn Tolentino, Brandon McWilliams, Kyu Cho, and Yongho Sohn. 2020. "Understanding the laser powder bed fusion of AlSi10Mg alloy." *Metallography, Microstructure, and Analysis* 9 (4): 484–502.

Jadhav, Suraj Dinkar, Louca Raphaël Goossens, Yannis Kinds, Brecht Van Hooreweder, and Kim Vanmeensel. 2021. "Laser-based powder bed fusion additive manufacturing of pure copper." *Additive Manufacturing* 42: 101990.

Karimi, P, Tahira Raza, Joel Andersson, and L-E Svensson. 2018. "Influence of laser exposure time and point distance on 75-μm-thick layer of selective laser melted Alloy 718." *The International Journal of Advanced Manufacturing Technology* 94 (5): 2199–2207.

King, W. E., H. D. Barth, V. M. Castillo, G. F. Gallegos, J. W. Gibbs, D. E. Hahn, C. Kamath, and A. M Rubenchik. 2014. "Observation of keyhole-mode laser melting in laser powder-bed fusion additive manufacturing." *Journal of Materials Processing Technology* 214 (12): 2915–2925.

Kurzynowski, Tomasz, Konrad Gruber, Wojciech Stopyra, Bogumiła Kuźnicka, and Edward Chlebus. 2018. "Correlation between process parameters, microstructure and properties of 316 L stainless steel processed by selective laser melting." *Materials Science and Engineering: A* 718: 64–73.

Lavery, NP, J Cherry, S Mehmood, H Davies, B Girling, E Sackett, SGR Brown, and J Sienz. 2017. "Effects of hot isostatic pressing on the elastic modulus and tensile properties of 316L parts made by powder bed laser fusion." *Materials Science and Engineering: A* 693: 186–213.

Letenneur, Morgan, Alena Kreitcberg, and Vladimir Brailovski. 2019. "Optimization of laser powder bed fusion processing using a combination of melt pool modeling and design of experiment approaches: Density control." *Journal of Manufacturing and Materials Processing* 3 (1): 21.

Li, Boyuan, Han Zheng, Changjun Han, and Kun Zhou. 2021. "Nanotwins-containing microstructure and superior mechanical strength of a Cu–9Al–5Fe–5Ni alloy additively manufactured by laser metal deposition." *Additive Manufacturing* 39: 101825.

Li, Ruidi, Jinhui Liu, Yusheng Shi, Li Wang, and Wei Jiang. 2012. "Balling behavior of stainless steel and nickel powder during selective laser melting process." *The International Journal of Advanced Manufacturing Technology* 59 (9): 1025–1035.

Liu, SY, HQ Li, CX Qin, R Zong, and XY Fang. 2020. "The effect of energy density on texture and mechanical anisotropy in selective laser melted Inconel 718." *Materials & Design* 191: 108642.

Mezghani, Adnen, Abdalla R Nassar, Corey J Dickman, Eduardo Valdes, and Raul Alvarado. 2021. "Laser powder bed fusion additive manufacturing of copper wicking structures: fabrication and capillary characterization." *Rapid Prototyping Journal* .

Mosa, Abdelkhalik, and Norman W Paton. 2016. "Optimizing virtual machine placement for energy and SLA in clouds using utility functions." *Journal of Cloud Computing* 5 (1): 1–17.

O'Regan, Paul, Paul Prickett, Rossi Setchi, Gareth Hankins, and Nick Jones. 2016. "Metal based additive layer manufacturing: variations, correlations and process control." *Procedia Computer Science* 96: 216–224.

Pfaff, Aron, Martin Jäcklein, Max Schlager, Wilfried Harwick, Klaus Hoschke, and Frank Balle. 2020. "An empirical approach for the development of process parameters for laser powder bed fusion." *Materials* 13 (23): 5400.

Pradeep, PI, A Akhilesh, V Anil Kumar, P Manikandan, K Naresh Kumar, T Venkateswaran, Ankit Sahu, Satish Kumar Singh, and P Ramesh Narayanan. 2021. "Characterization of Titanium Alloy Ti6Al4V-ELI Components made by Laser Powder Bed Fusion Route for Space Applications." *Transactions of the Indian National Academy of Engineering* 1–11.

Pragana, João PM, Pedro Pombinha, Valdemar R Duarte, Tiago A Rodrigues, João P Oliveira, Ivo MF Bragança, Telmo G Santos, Rosa M Miranda, Luísa Coutinho, and Carlos MA Silva. 2020. "Influence of processing parameters on the density of 316L stainless steel parts manufactured through laser powder bed fusion." *Proceedings of the Institution of Mechanical Engineers, Part B: Journal of Engineering Manufacture* 234 (9): 1246–1257.

Prashanth, Konda Gokuldoss, Sergio Scudino, Tapabrata Maity, J Das, and Jürgen Eckert. 2017. "Is the energy density a reliable parameter for materials synthesis by selective laser melting?" *Materials Research Letters* 5 (6): 386–390.

Promoppatum, Patcharapit, and Shi-Chune Yao. 2019. "Analytical evaluation of defect generation for selective laser melting of metals." *International Journal of Advanced Manufacturing Technology* 103.

Rao, Heng, Stephanie Giet, Kun Yang, Xinhua Wu, and Chris HJ Davies. 2016. "The influence of processing parameters on aluminium alloy A357 manufactured by Selective Laser Melting." *Materials & Design* 109: 334–346.

Rubenchik, Alexander M, Wayne E King, and Sheldon S Wu. 2018. "Scaling laws for the additive manufacturing." *Journal of Materials Processing Technology* 257: 234–243.

Scime, Luke, and Jack Beuth. 2019. "Melt pool geometry and morphology variability for the Inconel 718 alloy in a laser powder bed fusion additive manufacturing process." *Additive Manufacturing* 29: 100830.

Snow, Zackary, Abdalla Nassar, and Edward W Reutzel. 2020. "Review of the formation and impact of flaws in powder bed fusion additive manufacturing." *Additive Manufacturing* 101457.

Spears, Thomas G, and Scott A Gold. 2016. "In-process sensing in selective laser melting (SLM) additive manufacturing." *Integrating Materials and Manufacturing Innovation* 5 (1): 16–40.

Sun, Zhongji, Xipeng Tan, Shu Beng Tor, and Wai Yee Yeong. 2016. "Selective laser melting of stainless steel 316L with low porosity and high build rates." *Materials & Design* 104: 197–204.

Tang, M., P. C. Pistorius, and J. L. Beuth. 2017. "Prediction of lack-of-fusion porosity for powder bed fusion." *Additive Manufacturing* 14: 39–48.

Tang, Ming, Petrus Christiaan Pistorius, Colt Montgomery, and Jack Beuth. 2019. "Build Rate Optimization for Powder Bed Fusion." *Journal of Materials Engineering and Performance* 28 (2): 641–647.

Walsh, William E, Gerald Tesauro, Jeffrey O Kephart, and Rajarshi Das. 2004. "Utility functions in autonomic systems." In *International Conference on Autonomic Computing, 2004. Proceedings.*, 70–77. IEEE.

Wang, Di, Yang Liu, Yongqiang Yang, and Dongming Xiao. 2016. "Theoretical and experimental study on surface roughness of 316L stainless steel metal parts obtained through selective laser melting." *Rapid Prototyping Journal* .

Yan, Wentao, Yan Lu, Kevontrez Jones, Zhuo Yang, Jason Fox, Paul Witherell, Gregory Wagner, and Wing Kam Liu. 2020. "Data-driven characterization of thermal models for powder-bed-fusion additive manufacturing." *Additive manufacturing* 36: 101503.